# Role of telomere dysfunction in cardiac failure in Duchenne muscular dystrophy

Foteini Mourkioti[1], Jackie Kustan[1], Peggy Kraft[1], John W. Day[2], Ming-Ming Zhao[3], Maria Kost-Alimova[4], Alexei Protopopov[4], Ronald A. DePinho[5], Daniel Bernstein[3], Alan K. Meeker[6] and Helen M. Blau[1,7]

**Duchenne muscular dystrophy (DMD), the most common inherited muscular dystrophy of childhood, leads to death due to cardiorespiratory failure. Paradoxically, *mdx* mice with the same genetic deficiency of *dystrophin* exhibit minimal cardiac dysfunction, impeding the development of therapies. We postulated that the difference between *mdx* and DMD might result from differences in telomere lengths in mice and humans. We show here that, like DMD patients, mice that lack dystrophin and have shortened telomeres (*mdx/mTR*[KO]) develop severe functional cardiac deficits including ventricular dilation, contractile and conductance dysfunction, and accelerated mortality. These cardiac defects are accompanied by telomere erosion, mitochondrial fragmentation and increased oxidative stress. Treatment with antioxidants significantly retards the onset of cardiac dysfunction and death of *mdx/mTR*[KO] mice. In corroboration, all four of the DMD patients analysed had 45% shorter telomeres in their cardiomyocytes relative to age- and sex-matched controls. We propose that the demands of contraction in the absence of dystrophin coupled with increased oxidative stress conspire to accelerate telomere erosion culminating in cardiac failure and death. These findings provide strong support for a link between telomere length and dystrophin deficiency in the etiology of dilated cardiomyopathy in DMD and suggest preventive interventions.**

DMD is a lethal X-linked recessive disease that affects 1 in 3,500 live-born boys. DMD is characterized by severe progressive muscle wasting due to mutations in dystrophin, which links the inner cytoskeleton with the extracellular matrix and therefore plays a key role in plasma membrane integrity in both skeletal and cardiac muscles[1,2]. Loss of dystrophin destabilizes the membrane, which leads to increased muscle fragility and renders muscle cells highly susceptible to contraction-induced injury[3]. Although DMD is diagnosed on the basis of early skeletal muscle symptoms, progressive cardiorespiratory failure is the primary cause of death, generally in the third decade of life[4–7]. As the specific mechanisms underlying heart failure in DMD patients are poorly understood, present treatments entail supportive heart failure strategies such as administration of angiotensin-converting enzyme inhibitors and β-adrenergic blockers[8,9].

Crucial to our understanding of the molecular mechanisms that underlie the development of DMD and to the design of preventive and therapeutic regimens are animal models that are engineered with tissue-specific mutations that phenocopy the human disease. The most commonly used animal model of DMD is the *mdx* mouse, in which a nonsense mutation in the dystrophin gene eliminates expression of dystrophin[10]. Despite the absence of dystrophin in skeletal and cardiac muscles of *mdx* mice[10], these animals fail to recapitulate the hallmark features of DMD, including severe muscle weakness, progressive cardiomyopathy and shortened lifespan[6,7,11,12], severely limiting the utility of the model. A mouse model that more closely resembles the human disease would be invaluable, both for elucidating the pathophysiologic mechanism of cardiac failure in DMD and for the development of more efficacious therapies that target the heart.

A major difference between humans and laboratory mice is the length of their telomeres, specialized DNA–protein complexes comprised of tandem G-rich repeats and located at the ends of eukaryotic chromosomes, which serve to cap and protect chromosome ends[13]. For unknown reasons, telomere lengths differ among species, ranging from ∼5 to 15 kilobases (kb) in humans to >40 kb in mice[14,15]. Telomere shortening occurs during ageing and leads to uncapping, activating senescence and apoptotic programs that compromise the function of

organs with high rates of proliferation and turnover[16]. By deleting the RNA component TERC (mTR) of telomerase, mTR[KO] mice have been generated that are characterized by a progressive shortening of telomeres, which occurs in the germ line over successive generations (G1–G6). Indeed, ubiquitous shortening of telomeres by successive inbreeding of telomerase-deficient mice (*mTR*[KO]) reveals defects in a range of both proliferative and low-mitotic tissues, similar to what is seen in ageing humans[16].

Given the established link between telomere dysfunction and proliferative defects[16], we previously postulated that deficiency of a single key protein (such as dystrophin) might be unmasked in specific cell types (such as muscle) in mice with a moderately reduced telomere reserve (G1 or G2). We tested this hypothesis by crossing *mdx* mice with mice lacking the RNA component of telomerase (*mdx/mTR*[KO]). As predicted, telomere shortening depleted the proliferative stem cell reservoir that drives regeneration of damaged dystrophic skeletal muscles and the severe progressive muscle weakness typical of DMD was recapitulated[17].

Here we show that *mdx/mTR*[KO] mice manifest all of the classic signs of dilated cardiomyopathy and heart failure seen in DMD patients. In contrast to skeletal muscle, the heart is a largely quiescent tissue characterized by low cell turnover[18]. It therefore seemed counter-intuitive that a similar mechanism could drive the severe cardiomyopathy seen in DMD. Yet, we found that *mdx/mTR*[KO] mice at early generations (G1 and G2) are characterized by severe contractile and conductance dysfunction, ventricular dilation and early death.

A test of the clinical relevance of this model revealed that telomere lengths in cardiomyocytes from four DMD patients are 45% shorter than in cardiomyocytes of age- and sex-matched human controls. Together, these results highlight that in a setting of mild ubiquitous telomere shortening, the absence of a single contractile protein, dystrophin, elicits tissue-specific defects and significant telomere shortening in non-proliferative heart muscles. This leads to a cycle of DNA damage and telomere shortening, which in turn leads to accelerated organ failure due to mitochondrial dysfunction and oxidative stress. This finding led us to test treatments with antioxidants, which as predicted, delayed the progression of dilated cardiomyopathy and the onset of death in *mdx/mTR*[KO] mice. Our results provide insights into the cardiorespiratory defects specific to DMD patients and a murine model for testing treatments that will probably impact the quality of life and survival of patients.

## RESULTS

We generated dystrophic mice lacking telomerase activity by crossing *mTR*[Het] mice (lacking one copy of the RNA component of telomerase, known as *mTR* or *Terc*[19]) with the exon 53 dystrophin mutation known as C57BL6 *mdx*[4cv] (ref. 20; hereafter designated as *mdx*) as previously described[17]. Rigorous breeding strategies are critical to generate the appropriate controls and consistent phenotypes across generations (Supplementary Fig. S1a). Our breeding scheme yields *mdx/mTR*[KO] mice with a genetic background identical to control *mTR*[KO] mice, which is critical, as telomere length differs among mouse strains[15]. As the human disease is X-linked[21], our studies were restricted to male mice. Importantly, the cardiac dystrophic phenotype was compared in mice of all genotypes at the same age and generation, as telomere shortening increases in *mTR*[KO] mice with successive generations. Double-mutant

mice lacking dystrophin and telomerase at the first and second generation (*mdx/mTR*[G1] and *mdx/mTR*[G2], hereafter designated as G1 or G2, respectively) were compared with controls of the same generations: C57BL6 wild-type mice (WT), heterozygous mice *mdx/mTR*[Het] (Het; lacking dystrophin completely—hence *mdx*—and expressing one allele encoding TERC), and homozygous TERC-null mice (*mTR*[KO]).

### Cardiac dilation and premature death in G2 animals

DMD is characterized by a progressive dilated cardiomyopathy with left ventricular wall thinning and increased diameter[22]. Analysis of hearts from young (8- and 20-week-old) *mdx/mTR*[G2] (G2) mice revealed no obvious abnormalities in cardiac morphology (data not shown); however, by 32 weeks, increased left ventricle enlargement was evident in G2 hearts (Fig. 1a,b) relative to controls. Histologic and morphometric analysis of 32-week-old G2 hearts revealed extensive ventricular fibrosis (Fig. 1b,c) in agreement with reports that extensive fibrosis and scarring, generally localized to the wall of the left ventricle, are the most prevalent cardiac histological features in end-stage DMD patients[22]. Heart-to-body weight and heart-to-tibia length ratio measurements revealed minimal compensatory hypertrophy in G2 animals (Supplementary Fig. S1b), consistent with the human disease. Cardiomyocyte nuclear area was moderately reduced in G2 hearts (Supplementary Fig. S1d and e) and the cardiomyocyte diameter of G2 hearts was smaller than controls (Supplementary Fig. S1d and f). Organ-to-body weight ratios for other organs (lungs, testis, liver, spleen) were unaffected (Supplementary Fig. S1c). These data show that the dilated cardiomyopathy seen in G2 hearts is not due to a systemic effect associated with premature ageing and severe functional and anatomic deficits in multiple organs.

Kaplan–Meier survival analysis demonstrated that the lifespan of *mdx/mTR*[KO] mice is significantly reduced when compared with controls (Fig. 1d). Death first occurs at 30 weeks with a $t_{50}$ of 120 weeks in G1 mice and as early as 19 weeks of age with a $t_{50}$ of 80 weeks of age in G2 mice. In contrast, controls including WT, Het and *mTR*[G2], demonstrated a normal lifespan (Fig. 1d). Together, these data indicate that dystrophin deficiency in combination with critically shortened telomeres recapitulates the features of dilated cardiomyopathy and reduced lifespan seen in patients with DMD (ref. 22).

### Cardiac dysfunction in G2 animals

To assess cardiac function, echocardiography was performed. Left ventricular contractility of G2 mice, measured as the percentage of fractional shortening, was progressively impaired as a function of age. Echocardiograms for control and G2 mice showed no significant differences at 12 weeks (Supplementary Fig. S2a) and 20 weeks of age (Supplementary Fig. S2b), but by 32 weeks, G2 mice exhibited a significant reduction in fractional shortening relative to controls ($32 \pm 5\%$ versus $55 \pm 3\%$, respectively; Supplementary Fig. S2a and Videos S1). Two measurements of left ventricular size showed chamber dilation in G2 mice. Left ventricular transverse area in diastole was moderately increased in G2 mice relative to controls ($14 \pm 2 \, mm^2$ versus $8 \pm 2 \, mm^2$, respectively). Left ventricular transverse area in systole was also increased ($12 \pm 2 \, mm^2$ versus $4 \pm 2 \, mm^2$, respectively; Fig. 2a,b). Together these data show that cardiac contractile function is impaired and left ventricular chamber size is increased in G2 hearts. In addition, markers of cardiac failure, including atrial natriuretic
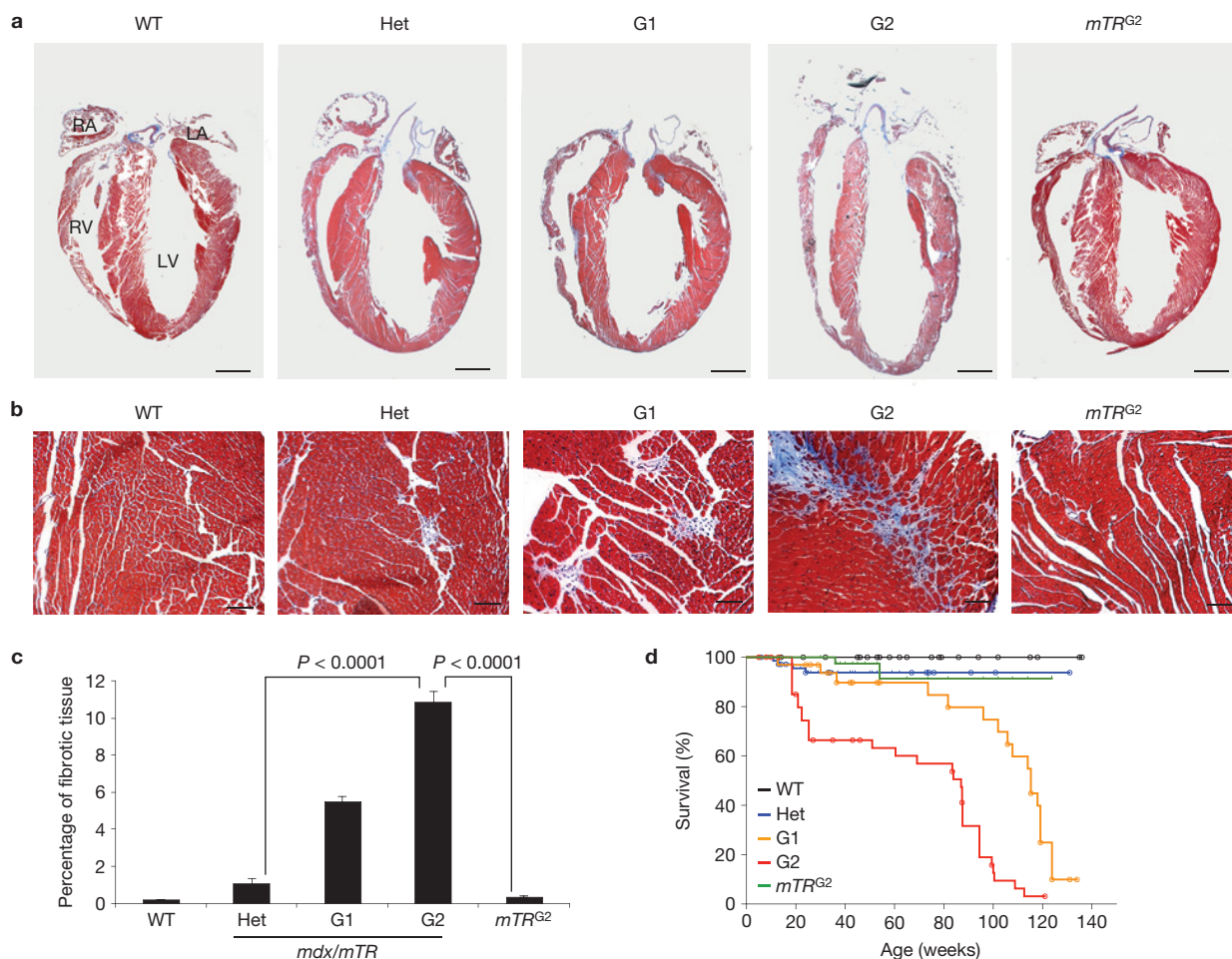
**Figure 1** Cardiac dilation, fibrosis and premature death in G2 mice. (**a**) Trichrome staining in longitudinal paraffin sections of 32-week-old hearts. G2 hearts develop dilated cardiomyopathy accompanied by enlarged ventricular cavity and thinning of the ventricular wall (LV, left ventricle; RV, right ventricle; LA, right atrium; RA, right atrium). Scale bars, 15 μm. (**b**) Increased collagen deposition (blue) in the left ventricle of G2 hearts compared with controls. Scale bars, 600 μm. (**c**) Quantification of collagen deposition. Data are represented as mean ± s.e.m. ($n = 3$–4), two-tailed, unpaired Student's $t$-test, $P$ values are indicated in the graph. (**d**) Kaplan–Meier survival curve shows that G2 mice have a significantly reduced lifespan when compared with controls. WT ($n = 72$), Het ($n = 86$), G1 ($n = 45$), G2 ($n = 53$) and $mTR^{G2}$ ($n = 45$). Source data are shown in Supplementary Table S1.

peptide (*Anp*) and brain natriuretic peptide (*Bnp*), were significantly elevated in G2 mice when compared with controls at 32 weeks (Fig. 2c), confirming progression to heart failure. Moreover, in response to stress (angiotensin II infusion), cardiac dysfunction was induced in younger G2 mice (Supplementary Fig. S3). Notably, although at 32 weeks, G1 mice have normal cardiac function (Fig. 2b), older G1 mice (80 weeks) have significantly reduced cardiac function (fractional shortening, left ventricular transverse area in diastole and left ventricular transverse area in systole) relative to controls (Supplementary Fig. S2c). In accordance, *mdx/mTR* mice at G3 (8 weeks) exhibit similar cardiac dysfunction much earlier than *mdx/mTR* mice at G2 (32 weeks; Supplementary Fig. S2c), indicating that telomere shortening plays an integral role in the cardiac functional defects.

Electrocardiograms (ECGs), a measure of cardiac electrical conduction, revealed delayed conduction in both G1 and G2 mice, evidenced by a wide QRS interval when compared with controls (Fig. 2d), indicating a significant ventricular depolarization defect in *mdx/mTR*^KO hearts, consistent with findings seen in DMD patients[23].

In contrast, age-matched WT, Het and *mTR*^G2 control mice had normal QRS durations (Fig. 2d), providing further evidence that the observed electrical dysfunction results from the combined impact of dystrophin and telomere dysfunction.

Magnetic resonance imaging (MRI) provides dynamic visualization of systolic myocardial wall thickening, and the extent of relaxation and contraction in diastole and systole, respectively[24]. The results of MRI analyses were in accordance with the data obtained by echocardiography and showed that G2 mice exhibit reduced left ventricular systolic function (Fig. 2e). Together, the impaired contractile function, detected by echocardiography and MRI, the prolonged depolarization evident by ECG, the increase in heart failure markers, and early mortality indicate that the hearts of G2 mice become progressively dysfunctional.

## Reduction in cardiomyocyte telomere length in G2 mice

To verify that cells within the hearts of G2 mice had shortened telomeres, we used a highly sensitive method for determining telomere
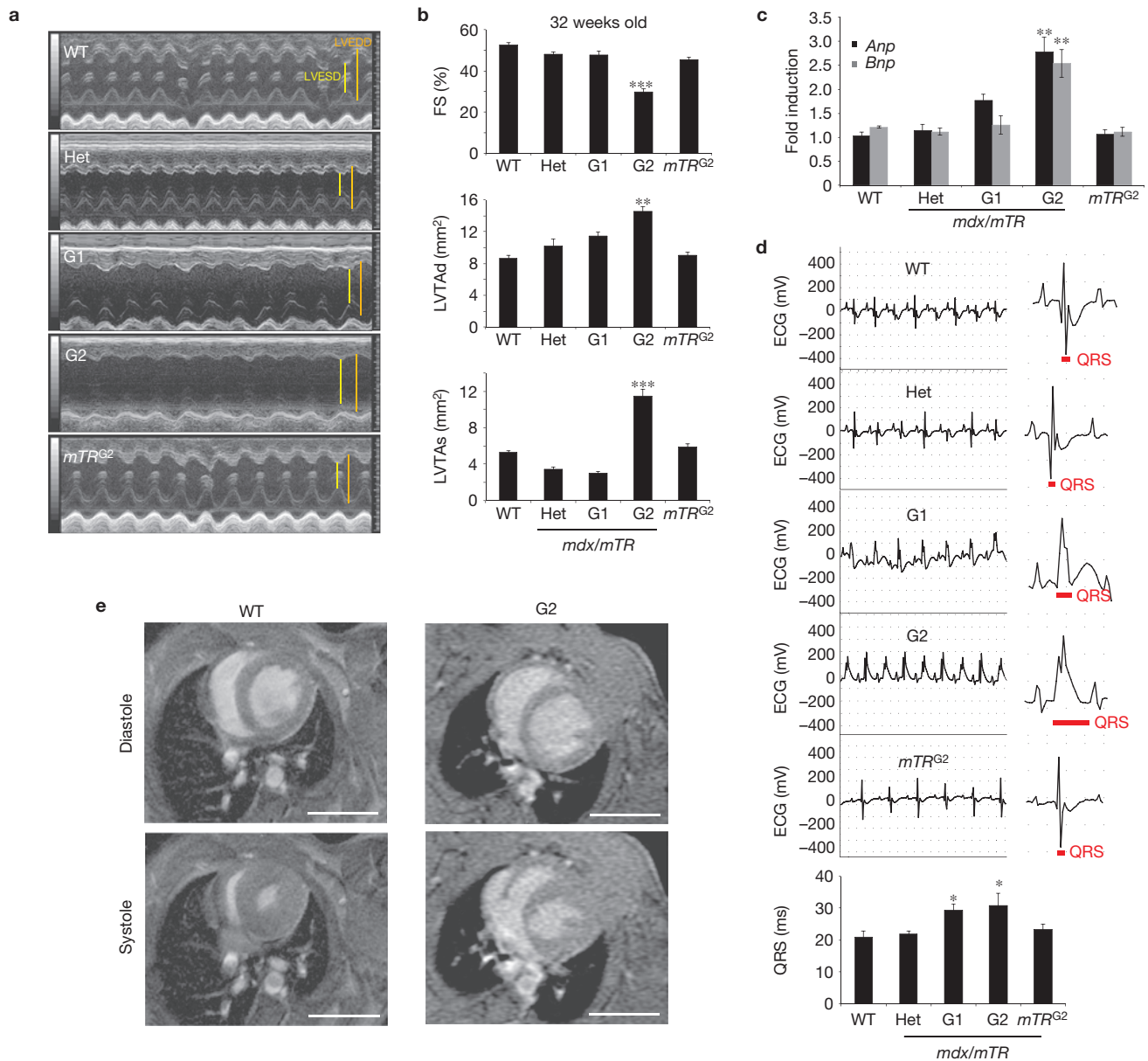
**Figure 2** Severe cardiac dysfunction and heart failure in G2 mice. (**a**) Representative images of 32-week-old hearts showing left ventricular dilation and compromised contractility (LVEDD, left ventricular end diastolic diameter; LVESD, left ventricular end systolic diameter). (**b**) Echocardiograph measurements show reduction in fractional shortening (FS), increase in left ventricular transverse area in diastole (LVTAd) and increase in left ventricular transverse area in systole (LVTAs) in 32-week-old G2 hearts compared with control hearts. Data are represented as mean ± s.e.m. ($n = 5$–8). Two-tailed, unpaired Student's $t$-test, $**P < 0.01$, $***P < 0.001$. (**c**) Increased cardiac failure markers atrial natriuretic peptide (*Anp*) and brain natriuretic peptide (*Bnp*) by quantitative rtPCR analysis confirmed heart failure in G2 mice. Data are represented as mean ± s.e.m. ($n = 3$). Two-tailed, unpaired Student's $t$-test, $**P < 0.01$. (**d**) Representative ECGs of 32-week-old hearts show impairment in ventricular depolarization of G1 and G2 hearts manifested by a prolonged QRS interval. Lower graph shows quantification of QRS values. Data are represented as mean ± s.e.m. ($n = 5$–9). Two-tailed, unpaired Student's $t$-test, $*P < 0.05$. (**e**) Representative MRI images at the level of the papillary muscle at diastole and systole confirms left ventricular chamber dilation and systolic dysfunction in G2 mice. Scale bars, 5 mm. Source data are shown in Supplementary Table S1.

length in tissue sections, telomere quantitative fluorescence *in situ* hybridization (telomere Q-FISH). This method has been used to obtain quantitative telomere length measurements both in murine[25,26] and human cells[27–29]. We optimized fixation methods that enabled telomere Q-FISH to measure telomere length in combination with immunostaining of a marker of cardiomyocytes (cardiac troponin T; Fig. 3a and Supplementary Fig. S4a). A highly significant 50% reduction in telomere length was evident in G2 cardiomyocytes relative to control

(WT, Het) and G1 cardiomyocytes (Fig. 3b). In contrast, control *mTR* at generation 2 (*mTR*^G2—lacking only TERC) cardiomyocytes exhibited a moderate reduction in telomere lengths, in agreement with studies by others[30,31], which do not report significant shortening until generations 4 and 5, demonstrating that the dystrophin mutation exacerbates telomere attrition.

To address whether telomere dysfunction in the smooth muscle of cardiac vessels contributes to the cardiac phenotype, we performed
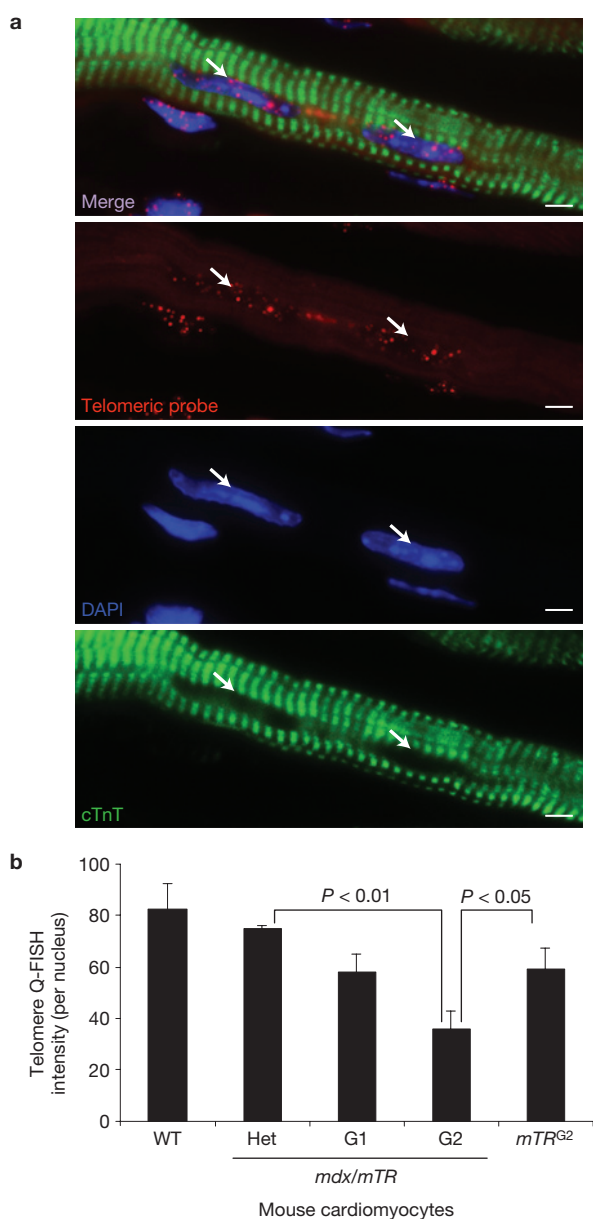
**Figure 3** Telomere Q-FISH analysis of cardiac sections from mice. (**a**) Representative telomere Q-FISH images (red telomeric probe; blue DAPI-stained nuclei; green immunofluorescence of cardiac troponin T (cTnT) reveals striated cardiomyocytes). White arrows indicate nuclei within cardiomyocytes. Scale bars, 400 μm. (**b**) Quantification of telomere shortening in cardiomyocytes represents the intensity sum of all telomere pixels (Cy3$^+$ telomeres) divided by the intensity sum of all nuclear DNA pixels of the entire nucleus (DAPI). A total of 3 hearts ($n = 3$) per genotype were analysed. The number of nuclei ($N$) scored: WT ($N = 394$), Het ($N = 303$), G1 ($N = 355$), G2 ($N = 414$), $mTR^{G2}$ ($N = 390$). Data are represented as mean ± s.e.m. Two-tailed, unpaired Student's $t$-test, $P$ values are indicated. Source data are shown in Supplementary Table S1.

telomere Q-FISH in combination with immunostaining of a marker of vascular smooth muscle, α-smooth muscle actin (Supplementary Fig. S4b,c). No significant differences in telomere lengths were evident in vascular smooth muscle cells of the different genotypes (Supplementary Fig. S4b,c). The standard control for Q-FISH was performed on testis (Supplementary Fig. S4d), as cell proliferation is

ongoing in this tissue and it is the first to show a reduction in telomere lengths or weight. In all genotypes (including $mdx/mTR^{G2}$ and $mTR^{G2}$), no significant differences were seen in telomere lengths (Supplementary Fig. S4e), tissue morphology[17] or organ weight (Supplementary Fig. S1c), indicating that global telomere shortening is not the basis for the observed phenotype. These data highlight that the enhanced telomere shortening is specific to cardiac (not smooth) muscle cells in the heart, and is not a systemic effect.

### Reduction in human cardiomyocyte telomere length in DMD hearts

To determine whether our findings in the mouse model were relevant to human DMD, we analysed post-mortem (<24 h) cardiac tissues from 4 DMD patients (13-, 15-, 17- and 19-year-old males). Telomere Q-FISH was performed in paraffin sections to assess telomere length in combination with immunostaining for the cardiac marker troponin T and nuclear DAPI stain (Fig. 4a and Supplementary Fig. S4f). Telomere lengths in human DMD cardiomyocytes were significantly reduced by 45%, ($P < 0.005$) when compared with cardiomyocytes from three post-mortem control hearts (20-, 25- and 30-year-old males without cardiac disease; Fig. 4b). Similar to what is seen in the $mdx/mTR$ mouse model, telomere Q-FISH combined with α-smooth muscle actin immunostaining (Supplementary Fig. S4g,h) demonstrated no significant difference in telomere length in the smooth muscle cells of cardiac vessels. These data validate the $mdx/mTR^{KO}$ mouse as a biologically relevant model of human DMD and provide evidence that telomere shortening in DMD patients is specific to cardiomyocytes.

### Telomere dysfunction combined with dystrophin mutation induces mitochondrial dysfunction and induces oxidative stress

Although increased cardiomyocyte proliferation or apoptosis did not account for the observed cardiac dysfunction (Supplementary Fig. S5), we observed profound mitochondrial aberrations. Mitochondrial compromise[31–33] and oxidative stress[34–37] have previously been implicated in myocardial dysfunction. Moreover, a strong link between telomere dysfunction and impairment of mitochondrial ultrastructure and organ function, indicative of ageing, was shown for liver and heart in mice lacking telomerase only at late generations (for example, G4; ref. 30). We therefore investigated the hypothesis that the dilated cardiomyopathy in mice at early generations (for example, G2) lacking telomerase and dystrophin is associated with mitochondrial dysfunction and oxidative stress. To assess whether telomere shortening in cardiomyocytes induces mitochondrial abnormalities in G2 mice, we performed electron microscopic analysis. Hearts from G2 animals exhibited multifocal abnormalities including a loss of thick as well as thin myofilaments (Fig. 5a), and a moderately increased number of mitochondria (data not shown) combined with decreased mitochondrial size (Fig. 5b). Most notably, the morphology of the mitochondria was highly aberrant, evident by the extensive fragmentation of mitochondria in G2 relative to control mice and lack of well-defined cristae (Fig. 5a,b). Our data suggest that mitochondrial abnormalities are accelerated in G2 mice lacking both telomerase and dystrophin, and strongly correlate with the observed cardiac dysfunction leading to early cardiac failure.

To determine whether the mitochondrial aberrations evident in the hearts of G2 mice at 32 weeks of age were mediated by the
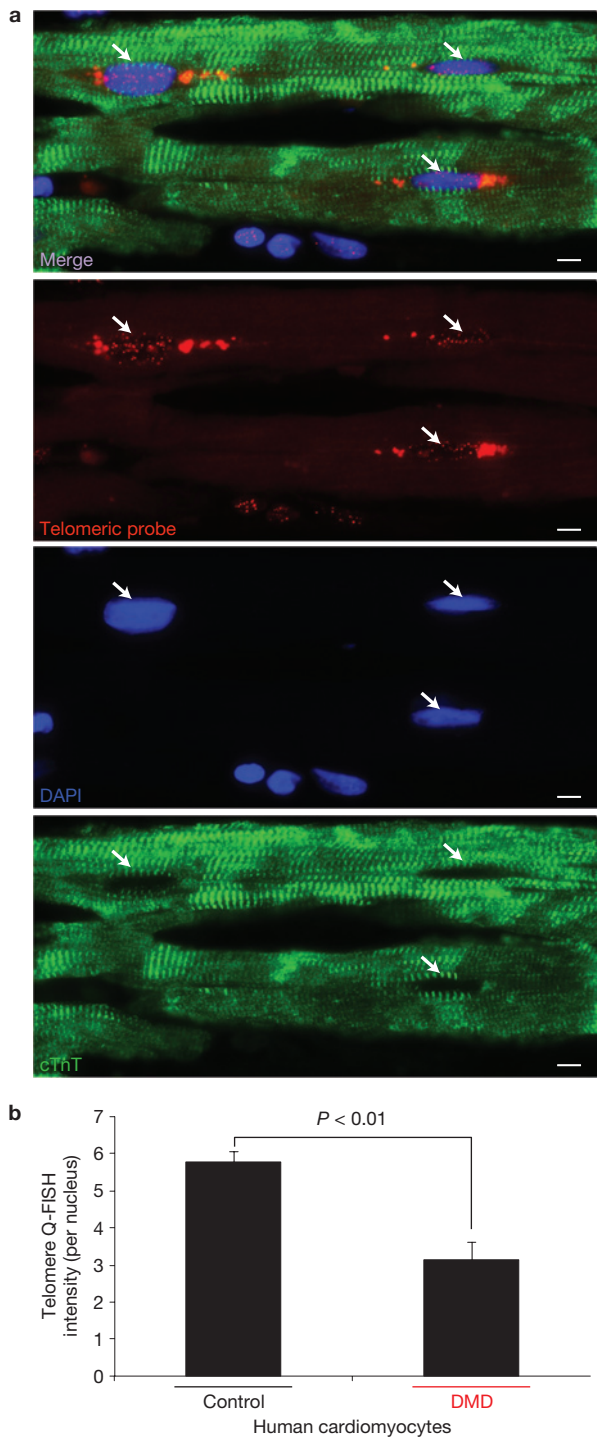
**b**



**Figure 4** Telomere Q-FISH analysis of cardiac section from human DMD hearts. (**a**) Representative telomere Q-FISH images (red, telomeric probe; blue, DAPI-stained nuclei; green, cardiac troponin T staining). Scale bars, 400 μm. (**b**) Quantification of telomere shortening in cardiomyocytes represents the intensity sum of all telomere pixels (Cy3+ telomeres) divided by the intensity sum of all nuclear DNA pixels of the entire nucleus (DAPI). A total of $n=3$ control and $n=4$ DMD cardiac samples were analysed and the number of nuclei ($N$) scored: Control 1 ($N=70$), Control 2 ($N=69$), Control 3 ($N=65$), DMD 1 ($N=42$), DMD 2 ($N=94$), DMD 3 ($N=65$) and DMD 4 ($N=72$). Data are represented as mean ± s.e.m. Two-tailed, unpaired Student's $t$-test, $P$ value is indicated. Source data are shown in Supplementary Table S1.

master mitochondrial regulators peroxisome proliferator activated receptor gamma co-activator 1 α (*Pgc1α*) and β (*Pgc1β*), we assayed their expression by quantitative real-time PCR (rtPCR). As expected, PGC1α and 1β levels were moderately diminished relative to control *mTR*^KO mice lacking telomerase only at generation 2 (∼50%), in agreement with a previous report[30]. Notably, however, expression levels of PGC1α and 1β in G2 mice lacking both telomerase and dystrophin (*mdx/mTR*^KO) were profoundly reduced (∼80%; Fig. 5c). These data indicate that the cardiac phenotype of mice lacking telomerase is exacerbated by the high metabolic demands of contraction in the absence of dystrophin.

To determine whether the mitochondrial compromise and dilated cardiomyopathy seen in G2 mice was accompanied by increased oxidative stress, we stained cardiac tissue sections for 8-hydroxy-deoxyguanosine (8-OHdG), a marker of oxidative damage[38–40]. A significant increase in the number of 8-OHdG-positive nuclei was detected in G2 hearts when compared with controls (Fig. 5d,e), indicating that oxidative stress is increased in G2 hearts. In agreement with this finding, expression of superoxide dismutase 1 and 2 (*Sod1* and *Sod2*), enzymes with an antioxidant function, were significantly decreased (Fig. 5f), providing further evidence of augmented oxidative stress in G2 hearts. Notably, mitochondrial function and oxidative stress are exacerbated by telomere dysfunction in combination with dystrophin mutation in G2 mice, leading to lethal cardiomyopathy.

## Amelioration of cardiac dystrophic phenotype after antioxidant treatment

To determine whether oxidative stress plays a role in the pathogenesis of G2 hearts, we subjected mice to two different antioxidants. The first (butylated hydroxyanisole (BHA); ref. 38) was administrated in the diet, and the second (Mn(III) tetrakis (4-benzoic acid) porphyrin chloride (MnTBAP), which specifically targets mitochondria[41]) was injected intraperitoneally daily (Fig. 6a). G2 mice treated with either antioxidant exhibited prolonged survival (Fig. 6b,e) and substantial amelioration of left ventricular function by echocardiography (fractional shortening; Fig. 6c,f and Supplementary Fig. S6d) relative to untreated G2 mice. MnTBAP was more potent than BHA by all functional measures and exhibited a reduction in fibrotic tissue and heart weight (Supplementary Fig. S6a,b,c). Moreover, transmission electron micrographs of longitudinal cardiac sections revealed improved mitochondrial cristae and morphology in MnTBAP-treated hearts when compared with saline-treated G2 controls (Fig. 6d). Together, these findings demonstrate that administration of antioxidants ameliorates both morphological and functional defects and significantly delays the progression of dilated cardiomyopathy in *mdx/mTR*^KO mice. These results suggest that the oxidative stress generated in the dystrophic heart is likely to play a causal role in cardiac dysfunction and is a potential early target for treatment in DMD patients.

## DISCUSSION

Patients with DMD typically die from cardiorespiratory failure, yet most therapeutic strategies in development at present target the skeletal muscles. Although generally diagnosed on the basis of skeletal myopathic symptoms, the cardiac defect warrants attention and early intervention. Fifty per cent of DMD patients 6–10 years of age exhibit abnormal ECGs (ref. 23) and by mid- to late-teenage years
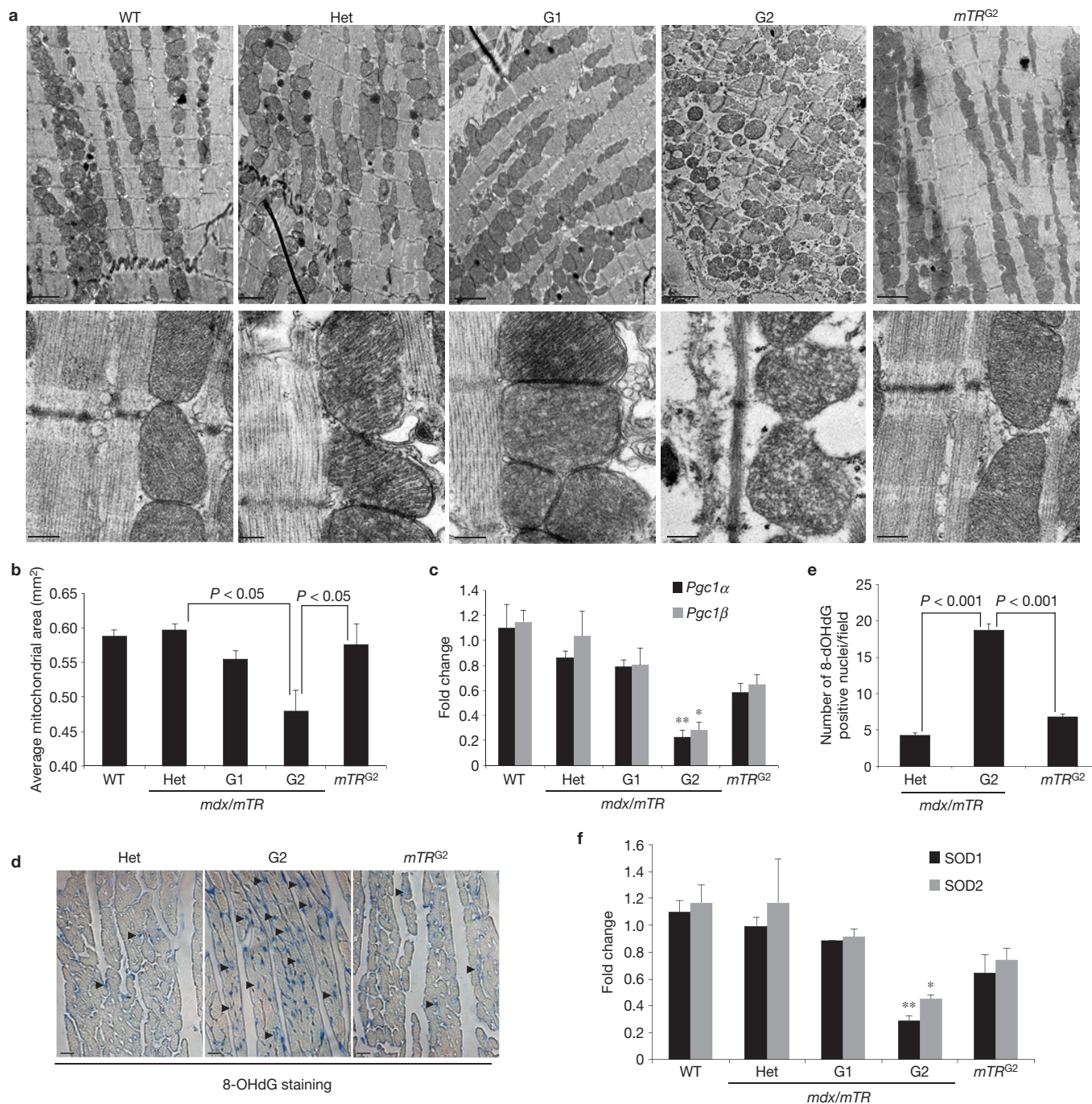
**Figure 5** Telomere dysfunction is associated with mitochondrial abnormalities and oxidative stress. (**a**) Top, representative longitudinal sections of murine cardiac muscle by transmission electron micrographs show cellular edema, loss of thick and thin filaments and mitochondrial fragmentation in G2 hearts compared with control images. Scale bars, 2 μm. Bottom, a closer look of mitochondria. Note the loss of cristae of G2 hearts. Scale bars, 0.2 μm. (**b**) Quantification of mitochondrial area ($n = 3$ animals per genotype, 3 different areas of the left ventricle per heart, and $n = 10$ photos per area analysed). Two-tailed, unpaired Student's $t$-test, $P$ values are indicated. (**c**) Quantitative rtPCR analysis for PGC1α and PGC1β gene expression show decreased levels in the G2 hearts ($n = 3$ hearts per genotype; data

are represented as mean ± s.e.m, two-tailed, unpaired Student's $t$-test, $^*P < 0.05$, $^{**}P < 0.01$). (**d**) Immunohistochemistry reveals increased number of 8-OHdG-positive nuclei in the hearts of 32-week-old G2 animals. Scale bars, 400 μm. (**e**) Quantification of the 8-OHdG staining. Data are represented as mean ± s.e.m ($n = 3$ hearts per genotype; > 10 images per heart were analysed). Two-tailed, unpaired Student's $t$-test, $P$ values are indicated. (**f**) Quantitative rtPCR analyses of levels of antioxidative enzymes (SOD1 and SOD2) show decreased levels in the hearts of G2 mice ($n = 3$ hearts per genotype; data are represented as mean ± s.e.m.). Two-tailed, unpaired Student's $t$-test, $^*P < 0.05$, $^{**}P < 0.01$. Source data are shown in Supplementary Table S1.

progressive cardiac dysfunction is common[4–7,23]. Hearts from DMD patients are often characterized by multifocal areas of degenerative changes, characterized by mitochondrial disorganization with loss or

discontinuity of cristae, fatty infiltration and loss of myofibres[23,42]. Virtually all DMD patients develop dilated cardiomyopathy and cardiac arrhythmia by the end of their lives[7]. As DMD patients now
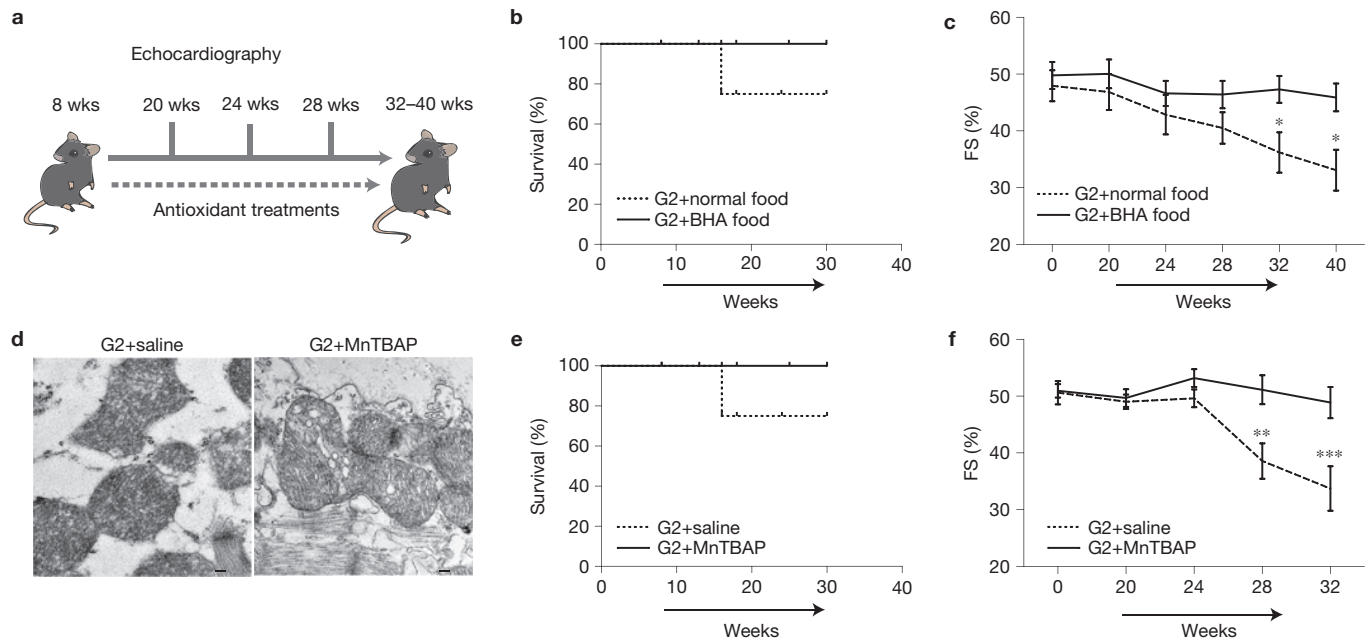
**Figure 6** Antioxidant treatment increased survival and improved cardiac function. (**a**) Scheme of experimental procedure. Mice were treated with antioxidant (BHA food or MnTBAP injection) at 8 weeks old and tested monthly for cardiac function by echocardiography until 32–40 weeks old. (**b**) Decreased mortality of G2 mice treated with BHA food. Animals tested: G2-BHA food ($n = 10$), G2-Normal food ($n = 10$). (**c**) Echocardiography measurements (by means of fractional shortening (FS) as a percentage) showed comparable increase in cardiac function of G2 mice treated with BHA food compared to controls. Analysis of variance followed by Bonferonni's test for multiple comparisons; $^*P < 0.05$.

(**d**) Representative longitudinal sections of murine cardiac muscle of MnTBAP-injected G2 hearts show improved mitochondria morphology. Note that some formation of cristae is evident in G2 MnTBAP-injected cardiac mitochondria. Scale bars, 0.2 μm. (**e**) Extension of survival in G2 mice treated with daily injections of MnTBAP. Animals tested: G2-MnTBAP ($n = 10$), G2-Saline ($n = 10$). (**f**) Improved cardiac function in MnTBAP-injected compared with saline-injected G2 hearts. Analysis of variance followed by Bonferonni's test for multiple comparisons; $^{**}P < 0.01$, $^{***}P < 0.001$. Source data are shown in Supplementary Table S1.

survive longer owing to increased options for supportive care[7,43], early treatments to prevent or limit the progressive dilated cardiomyopathy, which is now the leading cause of death, are highly desirable. However, the absence of a mouse model of DMD that faithfully mimics the pathophysiology of the human cardiomyopathy has limited our understanding of the underlying mechanisms and ability to test cardiac-specific therapies.

The development of a mouse model that recapitulates lethal human DMD has been hindered for decades, as *mdx* mice (dystrophin deficiency alone) have a surprisingly mild phenotype. A number of more severe dystrophic phenotypes have been created by breeding the *mdx* mouse with mice in which utrophin[44], MyoD (ref. 45), $\alpha_7$ integrin (ref. 46), α-dystrobrevin[47] or glycan processing[48] has been knocked out. These other mouse models have been instructive and highly useful in augmenting our knowledge of muscle development and pathophysiology, as well as serving as useful test systems for therapeutic interventions. However, these models[44–47] disrupt proteins essential for skeletal and/or cardiac muscle function that are not mutated or lost in DMD patients. An advantage of the *mdx/mTR*[KO] mouse model described here is that lack of dystrophin is coupled with shortened telomeres, as seen in humans with DMD. Mouse models that mimic other human genetic degenerative diseases[49,50] associated with DNA repair (ataxia telangiectasia) were first generated when bred with mice with shortened telomeres. Here we show that the *mdx* mouse manifests all of the main hallmarks of human DMD once bred with mice that lack telomerase (*mTR*) yielding *mdx* mice with shortened telomeres (*mdx/mTR*[KO]).

This report provides the first evidence for a cardiac phenotype in a mouse model of DMD and a conceptual basis for the disease mechanism. We previously reported that combined dystrophin and telomerase deficiency leads to a skeletal myopathy similar to that observed in human DMD, due to a chronic cycle of myofibre damage and repair that ultimately led to a loss of the stem cell reservoir due to the shortened telomeres[17,51]. Here we show that this model manifests essentially all features of cardiomyopathy described in DMD patients[7,22,52], including cardiac dilation, prolonged ventricular depolarization and decreased systolic function. We report ultrastructural changes in mitochondria, mitochondrial dysfunction including decreased levels of peroxisome proliferator-activated receptor γ and co-activator 1 α and β (*Pgc1α* and *1β*), and markers of oxidative compromise (decreased *Sod* and increased 8-OHdG) in *mdx/mTR*[KO] mice. Although these changes are typically associated with cardiomyopathy and heart failure of diverse etiologies[53,54] and shortened telomeres have also been detected in the hearts of patients with heart failure[55], this is the first report showing that these features can result from progressive telomere erosion, specifically in cardiomyocytes owing to the genetic absence of a single crucial cardiac-specific gene product. Notably, telomere shortening was not detected in other muscle cells of the heart, such as those of the vasculature, providing further support for the specificity of telomere dysfunction in cardiomyocytes in the etiology of the disease. These defects culminate in dilated cardiomyopathy and heart failure with an onset of death by 19 and 32 weeks of age, in G1 and G2, respectively. The importance of telomere

shortening in the etiology of dilated cardiomyopathy is underscored by our finding of shortened telomeres (45%) in the cardiomyocytes in four DMD patients (which lack dystrophin) when compared with controls (which express dystrophin).

Our data suggest that oxidative stress is a critical step in the pathogenesis of cardiac failure in patients with muscular dystrophy because antioxidants can ameliorate the main features of dilated cardiomyopathy and improve lifespan in our model. Moreover, although respiratory and skeletal muscle failure probably contribute to the observed cardiac phenotype, our findings highlight an intrinsic cardiac defect. On the basis of our results, we postulate that the *mdx/mTR*$^{G2}$ mouse model sets in motion a cycle whereby stress is initiated by the absence of dystrophin during continuous cycles of cardiac contraction in conjunction with short telomeres (already shortened in humans), which induces mitochondrial compromise and increased oxidative stress, which then leads to further telomere erosion and progression to lethal dilated cardiomyopathy. We postulate that as in DMD, shortened telomeres may well exacerbate other heritable tissue-specific protein deficits, as the long telomeres typical of mice may mask their manifestation. The findings reported here increase our understanding of DMD and will facilitate the development and testing of therapies targeted to treat or prevent the onset of heart failure and death. □

## METHODS

Methods and any associated references are available in the online version of the paper.

*Note: Supplementary Information is available in the online version of the paper*

### AUTHOR CONTRIBUTIONS
F.M. designed the studies and performed the experiments, J.K. performed mouse work, histology, immunohistochemistry, mitochondrial quantification analysis and design of schematic diagrams, P.K. maintained the mouse colony and performed histological sections, F.M., A.K.M., M.K-A. and R.A.D. aided with telomere analyses in mouse samples, F.M. and A.K.M. performed the telomere analysis in human samples, F.M. and D.B. performed the ECG analyses, F.M. and M-M.Z. performed the osmotic minipump experiments, J.W.D. provided human cardiac samples, and F.M. and H.M.B. designed the experiments, discussed and interpreted the results, and wrote the paper with input from A.K.M., R.A.D. and D.B.

1. Liew, C. C. & Dzau, V. J. Molecular genetics and genomics of heart failure. *Nat. Rev. Genet.* **5**, 811–825 (2004).
2. Hoffman, E. P., Brown, R. H. Jr & Kunkel, L. M. Dystrophin: the protein product of the Duchenne muscular dystrophy locus. *Cell* **51**, 919–928 (1987).
3. Petrof, B. J., Shrager, J. B., Stedman, H. H., Kelly, A. M. & Sweeney, H. L. Dystrophin protects the sarcolemma from stresses developed during muscle contraction. *Proc. Natl Acad. Sci. USA* **90**, 3710–3714 (1993).
4. Bushby, K., Muntoni, F. & Bourke, J. P. 107th ENMC international workshop: the management of cardiac involvement in muscular dystrophy and myotonic dystrophy. 7th–9th June 2002, Naarden, the Netherlands. *Neuromuscul. Disord.* **13**, 166–172 (2003).
5. Baxter, P. Treatment of the heart in Duchenne muscular dystrophy. *Dev. Med. Child Neurol.* **48**, 163 (2006).
6. Duan, D. Challenges and opportunities in dystrophin-deficient cardiomyopathy gene therapy. *Human Mol. Genet.* **15** (Spec No 2), R253–R261 (2006).
7. McNally, E. M. New approaches in the therapy of cardiomyopathy in muscular dystrophy. *Annu. Rev. Med.* **58**, 75–88 (2007).
8. Cohn, J. N. Heart failure: future treatment approaches. *Am. J. Hypertens.* **13**, 74S–78S (2000).
9. Cohn, R. D. *et al.* Angiotensin II type 1 receptor blockade attenuates TGF-β-induced failure of muscle regeneration in multiple myopathic states. *Nat. Med.* **13**, 204–210 (2007).
10. Bulfield, G., Siller, W. G., Wight, P. A. & Moore, K. J. X chromosome-linked muscular dystrophy (*mdx*) in the mouse. *Proc. Natl Acad. Sci. USA* **81**, 1189–1192 (1984).
11. Bridges, L. R. The association of cardiac muscle necrosis and inflammation with the degenerative and persistent myopathy of *MDX* mice. *J. Neurol. Sci.* **72**, 147–157 (1986).
12. Torres, L. F. & Duchen, L. W. The mutant *mdx*: inherited myopathy in the mouse. Morphological studies of nerves, muscles and end-plates. *Brain* **110** (pt 2), 269–299 (1987).
13. Greider, C. W. & Blackburn, E. H. The telomere terminal transferase of Tetrahymena is a ribonucleoprotein enzyme with two kinds of primer specificity. *Cell* **51**, 887–898 (1987).
14. Kipling, D. & Cooke, H. J. Hypervariable ultra-long telomeres in mice. *Nature* **347**, 400–402 (1990).
15. Hemann, M. T. & Greider, C. W. Wild-derived inbred mouse strains have short telomeres. *Nucleic Acids Res.* **28**, 4474–4478 (2000).
16. Lee, H. W. *et al.* Essential role of mouse telomerase in highly proliferative organs. *Nature* **392**, 569–574 (1998).
17. Sacco, A. *et al.* Short telomeres and stem cell exhaustion model Duchenne muscular dystrophy in *mdx/mTR* mice. *Cell* **143**, 1059–1071 (2010).
18. Bergmann, O. *et al.* Evidence for cardiomyocyte renewal in humans. *Science* **324**, 98–102 (2009).
19. Blasco, M. A. *et al.* Telomere shortening and tumor formation by mouse cells lacking telomerase RNA. *Cell* **91**, 25–34 (1997).
20. Im, W. B. *et al.* Differential expression of dystrophin isoforms in strains of *mdx* mice with different mutations. *Human Mol. Genet.* **5**, 1149–1153 (1996).
21. Emery, A. E. Population frequencies of inherited neuromuscular diseases—A world survey. *Neuromuscul. Disord.* **1**, 19–29 (1991).
22. Finsterer, J. & Stollberger, C. The heart in human dystrophinopathies. *Cardiology* **99**, 1–19 (2003).
23. Sanyal, S. K. & Johnson, W. W. Cardiac conduction abnormalities in children with Duchenne's progressive muscular dystrophy: electrocardiographic features and morphologic correlates. *Circulation* **66**, 853–863 (1982).
24. Schneider, J. E. *et al.* Fast, high-resolution *in vivo* cine magnetic resonance imaging in normal and failing mouse hearts on a vertical 11.7 T system. *J. Magn. Reson. Imaging* **18**, 691–701 (2003).
25. Flores, I. *et al.* The longest telomeres: a general signature of adult stem cell compartments. *Genes Dev.* **22**, 654–667 (2008).
26. Gonzalez-Suarez, E., Samper, E., Flores, J. M. & Blasco, M. A. Telomerase-deficient mice with short telomeres are resistant to skin tumorigenesis. *Nat. Genet.* **26**, 114–117 (2000).
27. Meeker, A. K. & De Marzo, A. M. Recent advances in telomere biology: implications for human cancer. *Curr. Opin. Oncol.* **16**, 32–38 (2004).

28. Meeker, A. K. *et al*. Telomere length assessment in human archival tissues: combined telomere fluorescence *in situ* hybridization and immunostaining. *Am. J. Pathol.* **160**, 1259–1268 (2002).

29. Meeker, A. K. *et al*. Telomere shortening occurs in subsets of normal breast epithelium as well as *in situ* and invasive carcinoma. *Am. J. Pathol.* **164**, 925–935 (2004).

30. Sahin, E. *et al*. Telomere dysfunction induces metabolic and mitochondrial compromise. *Nature* **470**, 359–365 (2011).

31. Brown, D. A. & O'Rourke, B. Cardiac mitochondria and arrhythmias. *Cardiovasc. Res.* **88**, 241–249 (2010).

32. Iglewski, M., Hill, J. A., Lavandero, S. & Rothermel, B. A. Mitochondrial fission and autophagy in the normal and diseased heart. *Curr. Hypertens. Rep.* **12**, 418–425 (2010).

33. Murdoch, C. E., Zhang, M., Cave, A. C. & Shah, A. M. NADPH oxidase-dependent redox signalling in cardiac hypertrophy, remodelling and failure. *Cardiovasc. Res.* **71**, 208–215 (2006).

34. Takimoto, E. *et al*. Oxidant stress from nitric oxide synthase-3 uncoupling stimulates cardiac pathologic remodeling from chronic pressure load. *J. Clin. Invest.* **115**, 1221–1231 (2005).

35. Van Empel, V. P. *et al*. Downregulation of apoptosis-inducing factor in harlequin mutant mice sensitizes the myocardium to oxidative stress-related cell death and pressure overload-induced decompensation. *Circ. Res.* **96**, e92–e101 (2005).

36. Sawyer, D. B. Oxidative stress in heart failure: what are we missing? *Am. J. Med. Sci.* **342**, 120–124 (2011).

37. Rasmussen, H. H., Hamilton, E. J., Liu, C. C. & Figtree, G. A. Reversible oxidative modification: implications for cardiovascular physiology and pathophysiology. *Trends Cardiovasc. Med.* **20**, 85–90 (2010).

38. Kratsios, P. *et al*. Antioxidant amelioration of dilated cardiomyopathy caused by conditional deletion of NEMO/IKK γ in cardiomyocytes. *Circ. Res.* **106**, 133–144 (2010).

39. Shigenaga, M. K., Gimeno, C. J. & Ames, B. N. Urinary 8-hydroxy-2'-deoxyguanosine as a biological marker of *in vivo* oxidative DNA damage. *Proc. Natl Acad. Sci. USA* **86**, 9697–9701 (1989).

40. Shirendeb, U. *et al*. Abnormal mitochondrial dynamics, mitochondrial loss and mutant huntingtin oligomers in Huntington's disease: implications for selective neuronal damage. *Human Mol. Genet.* **20**, 1438–1455 (2011).

41. Li, Y. *et al*. Cytosolic, but not mitochondrial, oxidative stress is a likely contributor to cardiac hypertrophy resulting from cardiac specific GLUT4 deletion in mice. *FEBS J.* (2011).

42. Sanyal, S. K., Johnson, W. W., Thapar, M. K. & Pitner, S. E. An ultrastructural basis for electrocardiographic alterations associated with Duchenne's progressive muscular dystrophy. *Circulation* **57**, 1122–1129 (1978).

43. Finder, J. D. *et al*. Respiratory care of the patient with Duchenne muscular dystrophy: ATS consensus statement. *Am. J. Respir. Crit. Care Med.* **170**, 456–465 (2004).

44. Deconinck, A. E. *et al*. Utrophin-dystrophin-deficient mice as a model for Duchenne muscular dystrophy. *Cell* **90**, 717–727 (1997).

45. Megeney, L. A. *et al*. Severe cardiomyopathy in mice lacking dystrophin and MyoD. *Proc. Natl Acad. Sci. USA* **96**, 220–225 (1999).

46. Rooney, J. E. *et al*. Severe muscular dystrophy in mice that lack dystrophin and α7 integrin. *J. Cell Sci.* **119**, 2185–2195 (2006).

47. Grady, R. M. *et al*. Role for α-dystrobrevin in the pathogenesis of dystrophin-dependent muscular dystrophies. *Nat. Cell Biol.* **1**, 215–220 (1999).

48. Chandrasekharan, K. *et al*. A human-specific deletion in mouse Cmah increases disease severity in the *mdx* model of Duchenne muscular dystrophy. *Sci. Transl. Med.* **2**, 42ra54 (2010).

49. Qi, L. *et al*. Short telomeres and ataxia-telangiectasia mutated deficiency cooperatively increase telomere dysfunction and suppress tumorigenesis. *Cancer Res.* **63**, 8188–8196 (2003).

50. Wong, K. K. *et al*. Telomere dysfunction and Atm deficiency compromises organ homeostasis and accelerates ageing. *Nature* **421**, 643–648 (2003).

51. Chamberlain, J. S. Duchenne muscular dystrophy models show their age. *Cell* **143**, 1040–1042 (2010).

52. Frankel, K. A. & Rosser, R. J. The pathology of the heart in progressive muscular dystrophy: epimyocardial fibrosis. *Hum. Pathol.* **7**, 375–386 (1976).

53. Esposito, L. A., Melov, S., Panov, A., Cottrell, B. A. & Wallace, D. C. Mitochondrial disease in mouse results in increased oxidative stress. *Proc. Natl Acad. Sci. USA* **96**, 4820–4825 (1999).

54. Narula, N. *et al*. Adenine nucleotide translocase 1 deficiency results in dilated cardiomyopathy with defects in myocardial mechanics, histopathological alterations, and activation of apoptosis. *JACC Cardiovasc. Imaging* **4**, 1–10 (2011).

55. Brouilette, S., Singh, R. K., Thompson, J. R., Goodall, A. H. & Samani, N. J. White cell telomere length and risk of premature myocardial infarction. *Arterioscler. Thromb. Vasc. Biol.* **23**, 842–846 (2003).

# METHODS

**Mice.** All protocols were approved by the Stanford University Administrative Panel on Laboratory Animal Care. C57BL6 mdx[4cv] mice[20] and C57BL6 mTR[Het] mice[19] were used to generate the double-mutant animals as described in Supplementary Fig. S1a. Genotyping was performed by PCR as described previously[17]. As the human disease is X-linked[21], our studies were restricted to male mice. The exact number of animals for each data set and all relevant details regarding the sample size are reported with each experiment.

**ECG analysis.** ECGs were recorded to assess intra-left-ventricle conduction using Chart for Windows v4.1 (AD Instruments, Colorado Springs) as described previously[56]. ECGs were recorded from needle electrodes inserted subcutaneously in the chest and secured with tape. If the ECG was abnormal, other positions were used to validate and/or further characterize the ECG abnormality. The signal was acquired for 1 min and in three different electrode chest positions per mouse. During offline analysis, we examined the 1 min recording for unusually shaped QRS and for time-varying phenomenon (for example, irregularities in interval durations). Ectopic or abnormal beats were noted. A representative 10–15 s segment of the recording was averaged to obtain the signal averaged ECG.

**Echocardiographic analysis.** Animals were anaesthetized with isoflurane (1.5% in $O_2$) and the left hemithorax was shaved. The mice were placed on a temperature-controlled pad and heart rate was continuously monitored (400–550 bpm). Ultrasound transmission gel (Parker Laboratories) was used and the heart was imaged in the parasternal short-axis view. Two-dimensional B-mode and M-mode images were obtained at the papillary muscle level using the Vevo 770 Ultrasound system (VisualSonics) and left ventricular transverse area in systole, left ventricular transverse area in diastole and fractional shortening were calculated using the using Vevo 770 V2.2.3 software (VisualSonics). All analyses were performed with the investigators blinded to genotype.

**Magnetic resonance imaging analysis.** Magnetic resonance imaging was performed at the Stanford Clark Center Small Animal Imaging Facility in a self-shielded Varian/General Electric microSigna 7.0 7T, 310 mm (horizontal) bore scanner (Varian, GE Healthcare), including Copley gradient drivers, EXCITE2 electronics, the supporting LX11 platform, and a custom-built quadrature birdcage radiofrequency coil. Animals were anaesthetized with 2% isoflurane in humidified medical-grade oxygen. Physiological respiration and temperature feedback was carefully monitored and cardiac acquisitions were gated to the cardiac cycle. The animal was placed on an animal bed while kept under anaesthesia. During the scan, the heart rate, respiration and ECG signals were monitored closely. Transverse cardiac images were acquired with a fast gradient echo sequence, a flip angle of 20°, repetition time of 200 ms, echo time of 0.9 ms, slice thickness of 1 mm, 3 cm field of view with a 256 × 256 matrix, and a number of excitations (averages) of 2. Image analysis was performed using the open source software Osirix (http://www.osirixviewer.com).

**Electron microscopy.** Samples were fixed in Karnovsky's fixative (2% glutaraldehyde (EMS) and 4% paraformaldehyde (EMS) in 0.1 M sodium cacodylate (EMS) at pH 7.4) for 1 h at room temperature, then cut, post-fixed in 1% osmium tetroxide (EMS) for 1 h at room temperature, washed 3 times with ultrafiltered water, and then en bloc stained for 2 h at room temperature or moved to 4 °C overnight. Samples were then dehydrated in a series of ethanol, followed by acetonitrile for 15 min. Samples were infiltrated with EMbed-812 resin (EMS) mixed 1:1 with acetonitrile for 2 h followed by 2 parts EMbed-812 to 1 part acetonitrile for 2 h. The samples were then placed into EMbed-812 for 2 h, then placed into moulds (and resin-filled gelatin capsules with labels were orientated properly) and placed into a 65 °C oven overnight. Sections were taken between 75 and 90 nm on a Leica Ultracut S (Leica) and grids were contrast stained for 15 min in 1:1 saturated UrAcetate (~7.7%) to 100% ethanol followed by staining in 0.2% lead citrate for 3 min. Photos were taken using a Gatan Orius digital camera.

**Chronic angiotensin administration.** Osmotic minipumps (Alzet 2004) filled either with angiotensin II (0.9 µg h$^{-1}$, Sigma A9525) or 0.9% saline were implanted subcutaneously into each mouse, as described previously[57].

**Cardiac morphology and morphometric analysis.** Hearts were excised at the indicated ages and fixed overnight in 4% paraformaldehyde. Following progressive tissue dehydration with ethanol and xylene, the heart samples were embedded in paraffin. Cross-sections (7 µm thick) were subjected to trichrome staining (Sigma-Aldrich) for nuclei, cytoplasm and collagen visualization. Images from randomly chosen fields distributed across the cardiac section were collected using a Zeiss stage microscope (AxionVision) and morphometric analysis for collagen tissue deposition was performed with MetaMorph software (version 6.2r5; Universal Imaging).

**Quantitative-rtPCR-based gene expression analysis.** Total RNA was isolated from hearts using TRIzol (Invitrogen). RNA was treated with DNaseI enzyme (Promega) for 1 h at 37 °C and then subjected to column purification (Qiagen). The RNA concentration was determined with a spectrophotometer. After RNA quality verification, 1 µg was used to prepare cDNA (Ready-To-Go, T-Primed First-Strand Kit, Amersham Bioscience 27-9263-01). Inventoried TaqMan FAM probes (Applied Biosystems) were used for the relative quantification of the mRNA levels of atrial natriuretic peptide (Anp) (Mm01255747$_g$1), brain natriuretic peptide (Bnp) (Mm00435304$_g$1), superoxide dismutase (Sod1) (Mm01344232$_g$1) and Sod2 (Mm00449726$_m$1), peroxisome proliferator-activated receptor gamma coactivator 1-α (Pgc1α) (Mm00447184$_g$1) and 1-β (Pgc1β) (Mm01258517$_g$1) genes. Taqman VIC glyceraldehyde 3-phosphate dehydrogenase (Gapdh) probes (4552339E) were used for normalization. Data analysis was performed using the $\Delta\Delta C(T)$ method.

**Immunofluorescence microscopy.** Slides were deparaffinized in xylene and re-hydrated in serial ethanol concentrations. Antigen masking was performed in citrate buffer (10 mmol l$^{-1}$ sodium citrate, pH 6.0) for 30 min in a pressure cooker. Slides were blocked with 5% normal goat serum (DAKO) for 1 h at room temperature. Incubation with primary antibody against 8-hydroxy-2′-deoxyguanosine (8-OHdG; 1:20, JaICA), activated caspase-3 (1:50, Abcam ab13847), smooth muscle α-actin (1:200, Abcam ab32575), α-actinin (1:200, Sigma A7811), phospho-Hist3 (1:50, Cell Signaling 9706) and Ki67 (1:100, Dako Clone TEC-3) was done overnight at 4 °C. After washing in PBS, the slides were incubated with the appropriate biotinylated secondary antibody for 60 min at room temperature (for 8-OHdG staining) or with the appropriate Alexa 488 or Alexa 596 secondary antibodies (1:500, Invitrogen) for 1.5 h in the dark at room temperature. The nuclei were counterstained with DAPI. The slides were again washed in PBS and incubated for 30 min with VECTASTAIN ABC-AP reagent (Vector Laboratories). Next, the Vector Blue Alkaline Phosphatase substrate kit was used (Vector Laboratories) to visualize the 8-OHdG staining (blue colour). Then, slides were dehydrated through serial ethanol concentrations and a xylene-free clearing reagent (National Diagnostics) and mounted permanently. Quantification of 8-OHdG-positive nuclei was performed in a blind fashion after acquisition of at least 5 images from the left ventricle of each sample ($n = 3$) at ×40 magnification. Background was reduced using brightness and contrast adjustments, and colour balance was performed to enhance colours. All of the modifications were applied to the whole image using Adobe Photoshop CS3.

**TUNEL assay.** Deparaffinized cardiac sections were permeabilized by proteinase K treatment for 30 min and re-fixed in 4% paraformaldehyde. After an equilibration step, the 3′-OH end of DNA breaks was labelled with fluorescein-12–dUTP using recombinant terminal deoxynucleotidyl transferase enzyme (Promega G3250) by incubating the slides at 37 °C for 1 h. The reaction was terminated in 2X SSC solution and the slides were washed in PBS and mounted with DAPI (Vectashield).

**Human cardiac tissue.** Control hearts were isolated <24 h post mortem from de-identified male patients aged 20, 25 and 30 years who succumbed to non-cardiac disease (metastatic sarcoma, sickle-cell anaemia, and chronic pancreatitis). The DMD hearts were isolated <24 h post mortem from de-identified 13- and 15-year-old (Harvard), 17-year-old (Johns Hopkins) and 19-year-old (University of Wisconsin) patients. All samples went through the routine neutral-buffered formalin fixation followed by paraffin embedding. Sections (4 µM) from the paraffin blocks were placed on ChemMate slides (Fisher Scientific) for the telomere Q-FISH analysis. All protocols using human samples were reviewed and approved by the Stanford Institutional Review Board.

**Telomere Q-FISH.** Sections (4 µM thick) of embedded paraffin hearts were cut and preheated to 65 °C for 10 min and passed through xylene to remove paraffin. Slides were hydrated through a graded ethanol series, deionized water and then immersed for 60 s in dH$_2$O with 1% Tween-20 detergent, followed by immersion in citrate buffer at pH 6.0 in a steamer for 35 min. After cooling, slides were immersed in dH$_2$O, 70% ethanol and 95% ethanol, and then allowed to dry at room temperature. Thirty-five microlitres of diluted PNA probe hybridization solution (0.3 µg ml$^{-1}$ Cy3-labelled telomere PNA and 0.3 µg ml$^{-1}$ FITC-labelled centromere PNA; both probes custom synthesized by Bio-Synthesis) was placed onto the specimen. After denaturation (84 °C, 5 min), slides were left overnight to hybridize (dark). Next, slides were washed twice with PNA wash solution (formamide, 1 M Tris at pH 7.5 and dH$_2$O) and PBST, and were blocked for 1 h with blocking solution (Invitrogen). Afterwards, slides were incubated for 1 h at room temperature with primary antibodies (anti-mouse α-cardiac troponin T (1:100, Abcam) or anti-rabbit α-smooth muscle (1:100, Abcam)), washed with PBST, incubated with secondary antibodies (anti-mouse IgG fraction Alexa Fluor 488 (Molecular Probes) or anti-rabbit IgG fraction Alexa Fluor 488 (Molecular Probes)) for 30 min, counterstained with 1 µg ml$^{-1}$ DAPI solution in dH$_2$O, washed

in dH$_2$O, air dried and mounted (Prolong, Molecular Probes). To avoid differences in day-to-day staining efficiency variation, Q-FISH and immuno-Q-FISH staining as well as the image capture were performed on the same day. To control for differences in ploidy and probe accessibility, FITC-labelled PNA probes were used that recognize centromeric major satellite repeats, as described previously[28,29]. DAPI staining was used to define nuclear area and for quantification of DNA content, and Cy3 staining was used to quantify telomere fluorescence. Telomere fluorescence signals for individual cells of interest were identified by overlay of the DAPI image. Omega Optical XF38 filter set (Omega Optical Incorporated) for Cy3 visualization was used as described in ref. 29. The range of focal planes was examined on the $Z$ axis to determine that cardiomyocyte nuclei were within the striated muscle. Images were acquired at ×40. The investigators were blinded to the genotype of the sections analysed. Data were analysed using the Telometer: Software for Telomere Counting as described previously at http://demarzolab.pathology.jhmi.edu/telometer/. The algorithm developed at Johns Hopkins performs subtraction of background noise of the entire image, distinction of the individual telomere spots, removal of halos and separation of conjoined telomeres. The program generated statistics on the entire region of the nucleus, as well as each individual telomere in the nucleus. Statistics returned include the intensity sum of all Cy3 telomere pixels for a given nucleus (proportional to telomere length) and the intensity sum of all DAPI pixels for the nucleus (proportional to total nuclear DNA content). By taking the ratio of the telomere intensity sum to the corresponding DAPI intensity sum one is able to compensate for ploidy differences as well as the variable fractions of nuclei present in the cutting plane of the tissue section.

**Antioxidant treatments.** The commonly used 2018 Global diet (Mucedola srl) was used as normal diet, whereas the antioxidant diet was the same 2018 Global diet only supplemented with 0.7% of the antioxidant compound butylated hydroxyanisole (BHA; Sigma). Both normal and antioxidant food were weighed every day to ensure similar food intake in all of the experimental groups of the animals. In a second experiment using the alternative antioxidant Mn(III) tetrakis (4-benzoic acid) porphyrin chloride (MnTBAP), mice were treated every day until 42 weeks of age with 10 mg kg$^{-1}$) MnTBAP intraperitoneally or saline vehicle. Antioxidant treatments were provided at 8 weeks of age and onwards. Animals were kept in single cages to correlate food reduction in the cage with caloric intake for each mouse. Water was provided daily in graduated bottles to monitor liquid reduction. Detailed monitoring of cardiac function by echocardiography was performed before and monthly during the antioxidant treatments. The experiment was terminated between 40 and 42 weeks of age and the hearts were examined at the histological and molecular level. For each treatment, at least 10 animals were tested per genotype and condition.

**Statistical analysis.** Values were expressed as mean ± s.e.m. and differences with $P$ value <0.05 were considered significant (*$P < 0.05$, **$P < 0.01$, ***$P < 0.001$). Comparisons between two groups were performed using Student's $t$-test (tail 2, type 2 or 3). Repeated measures experiments were analysed by analysis of variance followed by Bonferonni's post-hoc corrections. All statistical analyses were performed using Excel or GraphPad Prism software. Source data are shown in Supplementary Table S1.

56. Urashima, T. *et al.* Molecular and physiological characterization of RV remodeling in a murine model of pulmonary stenosis. *Am. J. Physiol. Heart Circ. Physiol.* **295,** H1351–H1368 (2008).
57. McCalmon, S. A. *et al.* Modulation of angiotensin II-mediated cardiac remodeling by the MEF2A target gene Xirp2. *Circ. Res.* **106,** 952–960 (2010).
58. Yin, F. C. P., Spurgeon, H. A., Rakusan, K., Myron, L. & Lakatta, W. E. G. Use of tibial length to quantify cardiac hypertrophy: application in the aging rat. *Am. J. Physiol. Heart Circ. Physiol.* **243,** H941–H947 (1982).
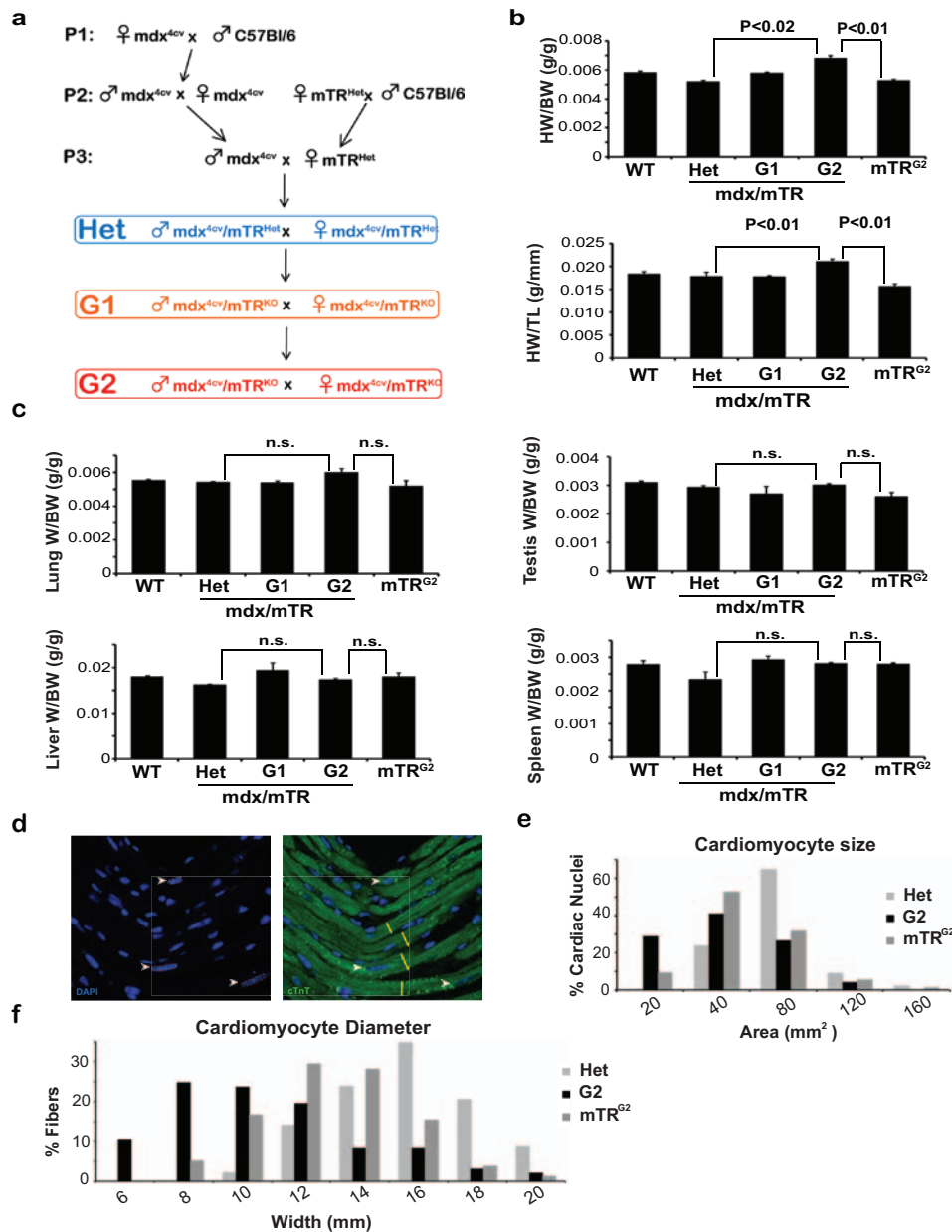
**Figure S1** Development of minimal hypertrophy in G2 mice and size of G2 cardiac muscle cells. **(a)** Breeding scheme describing the generation of mdx/mTR mice. Each C57BL6 *mdx*[4cv] (dystrophin mutations located on exon 53) or *mTR*[Het] (lacking the RNA component of telomerase), mouse is the result of isogenic breeding with C57BL6 wildtype (WT) mice from Jackson Laboratories to eliminate spontaneous mutations in the subsequent crosses. The resulting heterozygous mice (*mdx/mTR*[Het] designated as *Het*) were further intercrossed (intercousin matings only to preserve genetically uniform mice) to generate the first generation of double-mutant mdx mice totally lacking dystrophin and telomerase activity (*mdx/mTR*[G1] designated as G1). G1 mice were intercrossed (cousin matings only) to produce second-generation double mutant mice (mdx/mTR[G2] designated as G2). **(b)** Cardiac tissues were weighed from mice at 32 weeks of age. Data are represented as the weight of the tissue divided by the weight of the whole mouse, a standard control for telomere shortening [16]. Left graph shows comparison of heart to whole body weight (HW/BW) and right graph shows comparison of heart weight to tibial length (HW/TL), standard measurements of progressive development of cardiac dilation [56]. Data are represented as mean ±SEM. (n=3-5). Two-tailed, unpaired Student's *t*-test, P values are indicated. **(c)** Highly proliferative organs with substantial cell turnover, such as testis, liver, spleen and lung do not display significant differences in weight at G2. Data are represented as mean ±SEM (n=3-5); Two-tailed, unpaired Student's *t*-test, P> 0.2 (n.s.). **(d)** Representative image of nuclei (blue, DAPI, left panel) and cardiac myofibers (green, cTnT, right panel). These sections were used for the nuclei measurements. A total of 3 hearts per genotype were analyzed. **(e)** Histogram reveals a small decrease in the size of cardiac nuclei of G2 mice compared to controls. Number of measured nuclei: *mdx/mTR*[Het] (Het) (N=102), *mdx/mTR*[G2] (G2) (N=134) and *mdx/mTR*[G2] (N=97). **(f)** Morphometric analysis (frequency distribution of the diameter of cardiac fibers) show that G2 fibers are thinner that controls. Number of fibers scored: *mdx/mTR*[Het] (Het) (N=88), *mdx/mTR*[G2] (G2) (N=98) and *mTR*[G2] (N=96). Source data are shown in Supplementary Table S1.

**a** **12 weeks old**



**b** **20 weeks old**



**c**
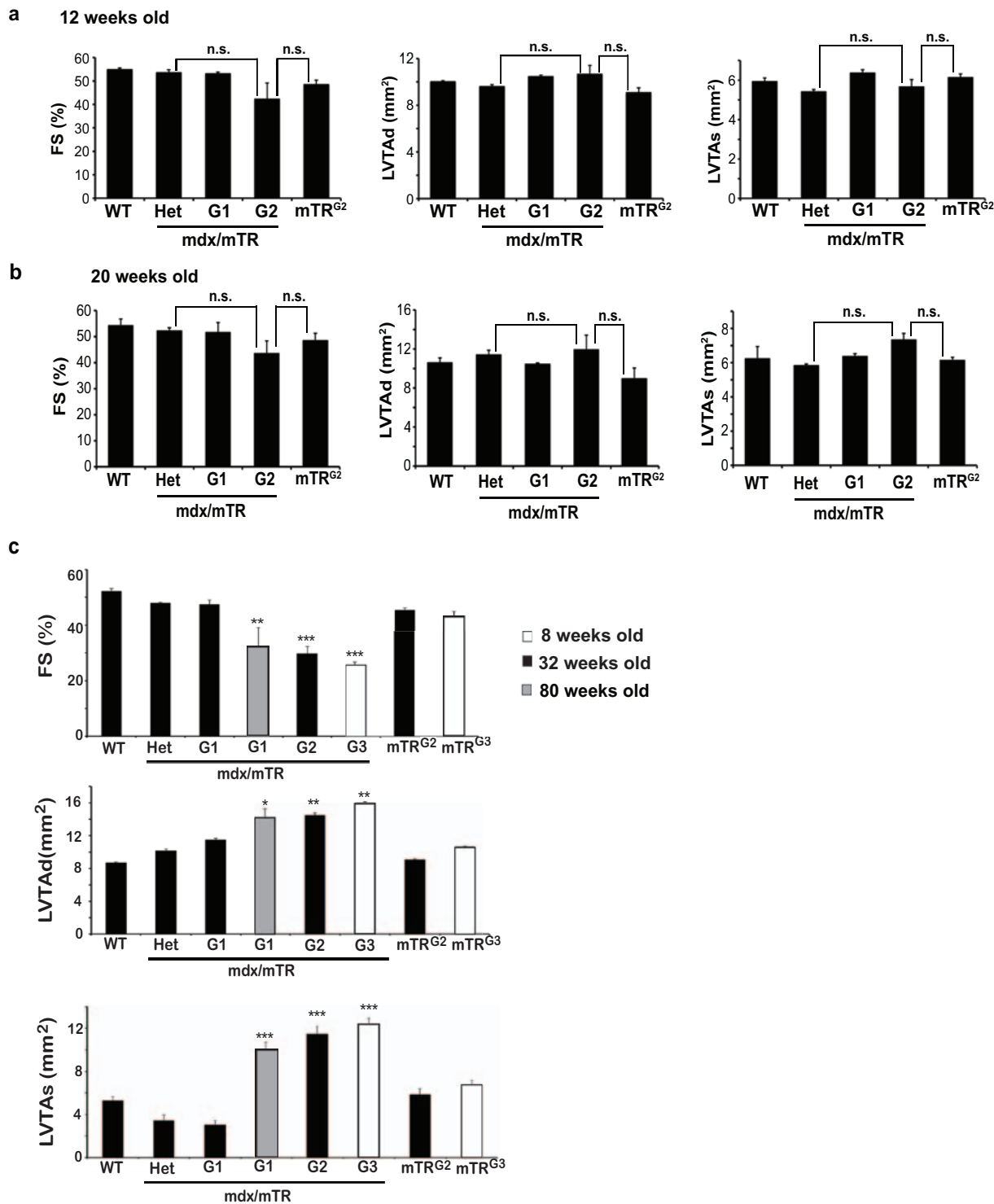


**Figure S2** Echocardiography measurements show similar measurements in young G2 animals, but significant differences in old G1 and young G3 animals. **(a-b)** No major differences in fractional shortening (%FS), Left Ventricular Transverse Area in diastole (LVTAd) and systole (LVTAs). (n=4-9) of **(a)** 12- **(b)** and 20-weeks-old mice. Two-tailed, unpaired Student's *t*-test, P>

0.1 (n.s.). **(c)** Cardiac dysfunction is evident in 80-weeks-old G1 animals (grey bars) and young 8-weeks-old G3 mice (white bars) compared to 32-weeks-old (black bars) animals. Data are represented as mean ±SEM (n=5-8); Two-tailed, unpaired Student's *t*-test, * indicates P <0.05, ** P<0.02 and *** P<0.001. Source data are shown in Supplementary Table S1.

**Figure S3** Angiotensin II induced stress induces premature heart failure in young G2 mice **(a)** Scheme of experimental procedure. Mice were tested for cardiac function by echocardiography prior to minipump insertion. Osmotic minipumps delivering either saline (S) or Angiotensin II (A) were implanted subcutaneously into 12-week-old asymptomatic G2 and control mice and cardiac function was measured weekly. **(b)** Representative images 3 weeks after minipump insertion show left ventricular dilation and compromised contractility only in G2 hearts that received Angiotensin II (See also Supplementary Video 2) **(c)** Echocardiographic measurements over time show reduction in fractional shortening (FS), increase in left ventricular transverse area in diastole (LVTAd) and increase in left ventricular transverse area in systole (LVTAs), only in hearts of G2 animals with Angiotensin II, compared to the control mice. Data are represented as mean ± SEM (n=5-6); ANOVA followed by Bonferonni test for multiple comparisons, ** indicates $P < 0.01$ and ***$P < 0.001$. **(d)** Representative histological analysis using Trichrome staining on longitudinal paraffin sections show increased fibrotic tissue deposition in hearts of Angiotensin II treated G2 mice compared to controls. **(e)** Quantification of fibrosis. Data are represented as mean ± SEM (n=4); Two-tailed, unpaired Student's $t$-test, P value is indicated. Source data are shown in Supplementary Table S1.
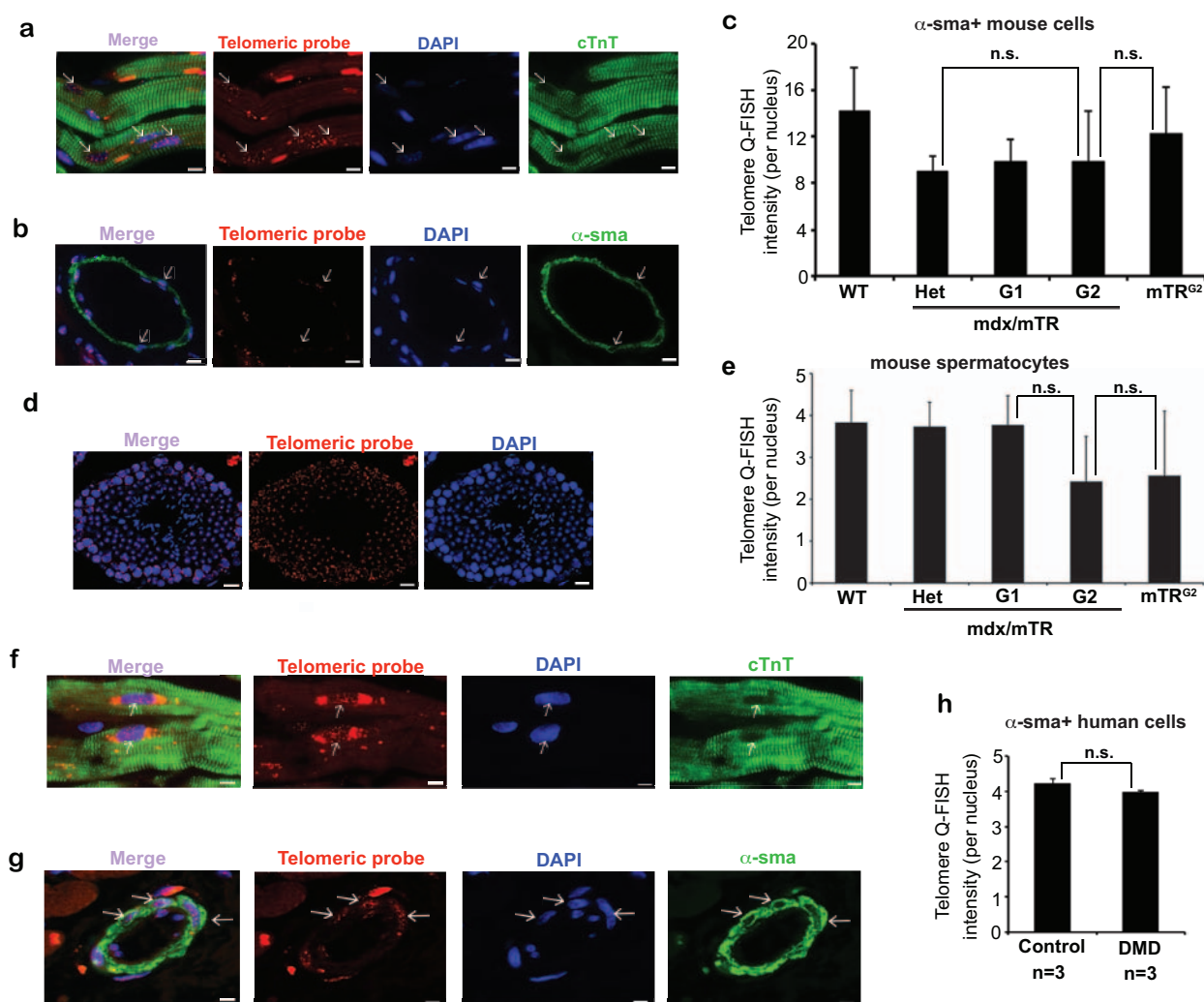
**Figure S4** Telomere Q-FISH analysis of mouse and human DMD hearts. **(a)** Representative Telomere Q-FISH images (red telomeric probe; blue DAPI-stained nuclei, and green immunofluorescence of cardiac Troponin T reveals striated cardiomyocytes). White arrows indicate nuclei within cardiomyocytes. DAPI staining was used to define nuclear area and Cy3 staining was used to quantify telomere fluorescence. Each Cy3 image was an overlay of the DAPI image. The nuclei within cardiomyocytes (as defined by cardiac Troponin T) were selected in the DAPI images and the Telometer program automatically calculated the pixels (Cy3+ telomeres) on the selected nuclei. **(b)** Representative Telomere Q-FISH images (red telomeric probe, blue DAPI-stained nuclei, and green immunofluorescence of α-smooth muscle cells reveals cardiac vessels). **(c)** Quantification of telomere shortening in α-smooth muscle mouse cells represents the intensity sum of all telomere pixels (Cy3+ telomeres) divided by the intensity sum of all nuclear DNA pixels of the entire nucleus (DAPI). n=3 hearts per genotype analyzed. The number of nuclei scored: WT (N=290), Het (N=140), G1 (N=195), G2 (N=186), mTR$^{G2}$ (N=282). Data are represented as mean ± SEM; Two-tailed, unpaired Student's t-test, P> 0.7 (n.s.), **(d)** Representative

Telomere Q-FISH mouse testis images (red, telomeric probe, blue DAPI-stained nuclei). **(e)** Quantification of the telomere shortening in the mouse testes' spermatocytes of all different genotypes. n=3 testes per genotype analyzed. The number of nuclei scored: WT (N=359), Het (N=320), G1 (N=300), G2 (N=221), mTR$^{G2}$ (N=219). Data are represented as mean ± SEM. Two-tailed, unpaired Student's t-test, P> 0.3 (n.s.). **(f)** Representative human Telomere Q-FISH images (red, telomeric probe; blue, DAPI-stained nuclei and green, cardiac Troponin T staining). **(g)** Representative human Telomere Q-FISH images (red telomeric probe, blue DAPI-stained nuclei, and green immunofluorescence of α-smooth muscle cells reveals cardiac vessels). **(h)** Quantification of telomere shortening in α-smooth muscle cells in human hearts represents the intensity sum of all telomere pixels (Cy3+ telomeres) divided by the intensity sum of all nuclear DNA pixels of the entire nucleus (DAPI). A total of 3 control and 3 DMD cardiac samples were analyze and the number of nuclei scored: Control 1 (N=43), Control 2 (N=35), Control 3 (N=52), DMD 2 (N=76), DMD 3 (N=41) and DMD 4 (N=58). Two-tailed, unpaired Student's t-test, P> 0.06 (n.s.). Source data are shown in Supplementary Table S1.

**a**



**b**

**Proliferating Cardiomyocytes**



**c**



**d**

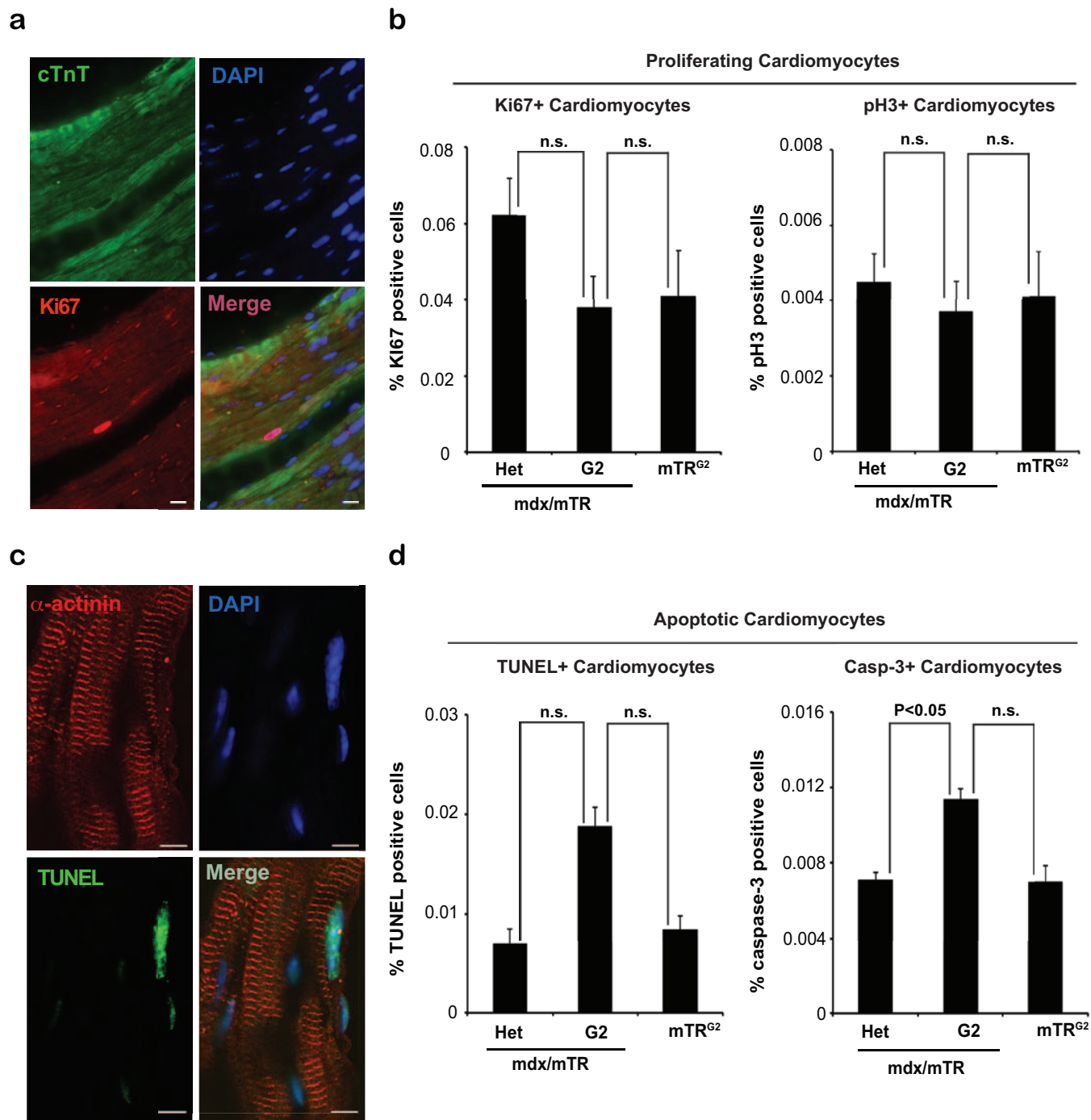**Apoptotic Cardiomyocytes**



**Figure S5** Cardiomyocyte proliferation and death in G2 hearts. **(a)** Representative image (red Ki67; blue DAPI-stained nuclei, and green immunofluorescence of cardiac Troponin T reveals striated cardiomyocytes) used to assess cardiac proliferation measurements. **(b)** No major differences on cardiomyocytes proliferation are detected by Ki67 (left graph) and phospho-Histone-3 (right graph) analysis. A total of 8-10 hearts per genotype were analyzed. Two-tailed, unpaired Student's t-test, P> 0.08 (n.s.). **(c)**

Representative image (green TUNEL; blue DAPI-stained nuclei, and red immunofluorescence of cardiac Troponin T reveals striated cardiomyocytes) used to assess cardiac apoptosis measurements. **(d)** Increase on cardiomyocytes apoptosis is detected by TUNEL (left graph) and cleaved caspase-3 (right graph) analysis. Data are represented as mean ±SEM (n=3); Two-tailed, unpaired Student's t-test, P values are indicated. Source data are shown in Supplementary Table S1.
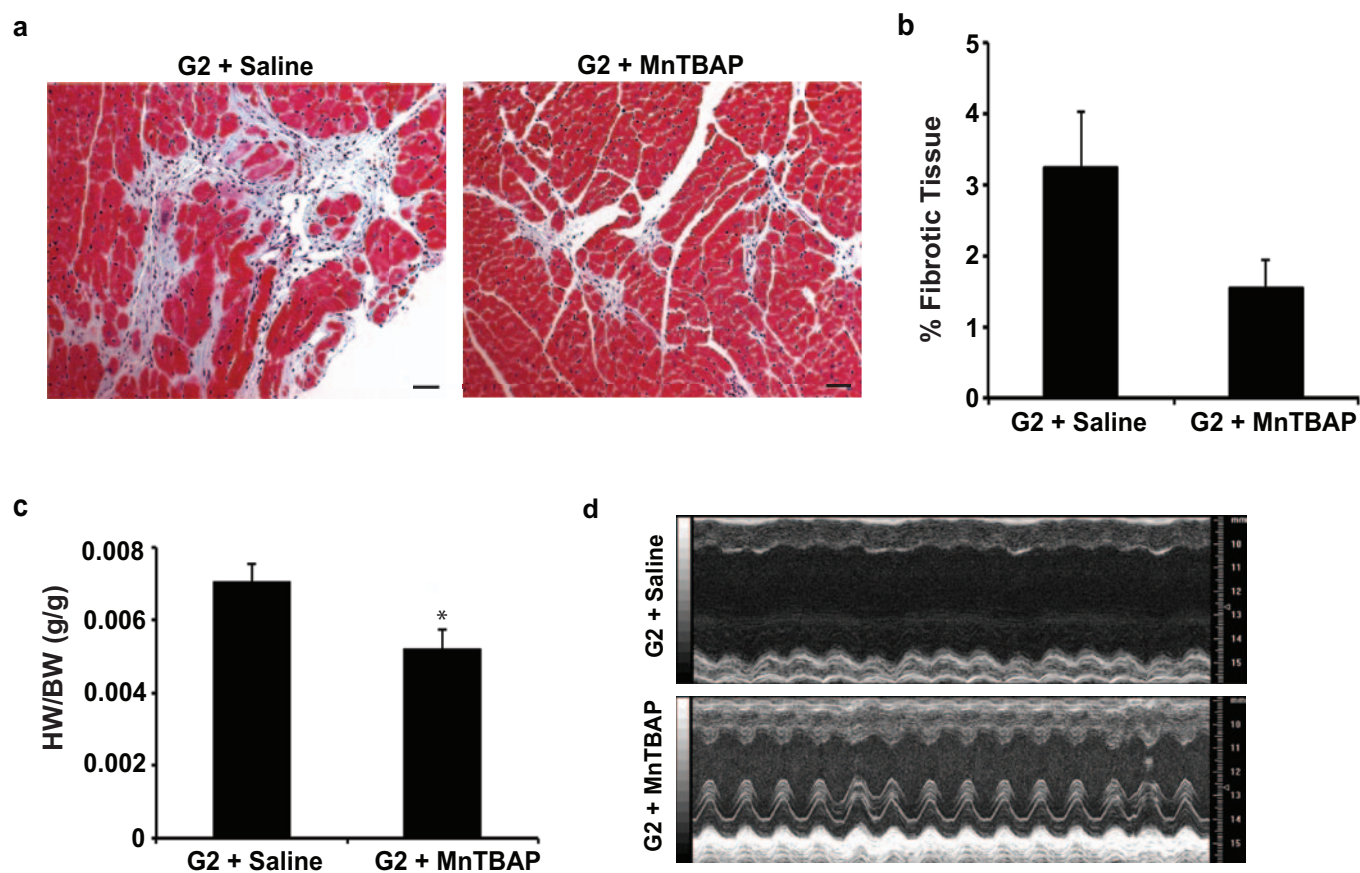
**Figure S6** Decreased cardiac fibrosis and dysfunction in anti-oxidant treated G2 animals. **(a)** Representative Trichrome staining of cardiac sections of G2-saline (left) and G2-MnTBAP injected hearts. The fibrosis of hearts from G2-MnTBAP injected mice is still present but significant reduced compared to controls. **(b)** Quantification of fibrosis. (n=5 mice per condition). Two-tailed, unpaired Student's *t*-test, P> 0.07 (n.s.). **(c)** Comparison of heart to whole body weight (HW/BW) at 32 weeks. Data are represented as mean ±SEM (n=6-7); Two-tailed, unpaired Student's *t*-test,* indicates P <0.05. **(d)** Representative images from G2-saline and G2-MnTBAP hearts showing restoration of left ventricular dilation and contractility. Source data are shown in Supplementary Table S1.

**Supplementary Videos**

**Video S1. Echocardiographic analysis indicate defect in G2 hearts.** Representative movies from 32-week old animals show increased LV size and impairment in ventricular function in G2 hearts.

**Video S2 Cardiac defect in G2 mice that received Angiotensin II.** Representative movies 3 weeks after the miniosmotic pump experiment from 12-week old *mdx/mTR*<sup>*Het*</sup> (Het) and G2 hearts received either saline or AngII. Note that the G2 hearts with AngII show left ventricular dilation, thin myocardial wall and compromised contraction.

**Supplementary Tables**

**Supplementary Table S1. Statistics Source Data.** This Table includes raw data values, descriptive statistics and p values for all experiments.